

On water delivery in the inner solar nebula

Monte Carlo simulations of forsterite hydration

M. D'Angelo^{1,2}, S. Cazaux^{3,4}, I. Kamp², W.- F. Thi⁵ and P. Woitke⁶

¹ Zernike Institute for Advanced Materials, University of Groningen, P.O. Box 221, 9700 AE Groningen, The Netherlands, e-mail: dangelomartinka@gmail.com

² Kapteyn Astronomical Institute, University of Groningen, P.O. Box 800, 9747 AV Groningen, The Netherlands, e-mail: kamp@astro.rug.nl

³ Faculty of Aerospace Engineering, Delft University of Technology, Delft, The Netherlands

⁴ University of Leiden, P.O. Box 9513, NL, 2300 RA, Leiden, The Netherlands

⁵ Max Planck Institute for Extraterrestrial Physics, Gießenbachstrasse 1, 85741 Garching, Germany

⁶ SUPA, School of Physics & Astronomy, University of St. Andrews, North Haugh, St. Andrews KY16 9SS, UK

September 6, 2018

ABSTRACT

Context. Endogenous or exogenous, dry or wet, various scenarios have been so far depicted for the origin of water on our Solar System's rocky bodies. Hydrated silicates found in meteorites and in interplanetary dust particles together with observations of abundant water reservoirs in the habitable zone of protoplanetary disks are evidences that support aqueous alteration of silicate dust grains by water vapor condensation in a nebular setting.

Aims. We investigate the thermodynamics (temperature and pressure dependencies) and kinetics (adsorption rates and energies, surface diffusion and cluster formation) of water adsorption on surfaces of forsterite grains, constraining the location in the solar nebula where aqueous alteration of silicates by water vapor adsorption could occur efficiently and lead to the formation of phyllosilicates. We analyze the astrophysical conditions favorable for such hydration mechanism and the implications for water on solid bodies.

Methods. The protoplanetary disk model (ProDiMo) code is tuned to simulate the thermochemical disk structure of the early solar nebula at three evolutionary stages. Pressure, temperature and water vapor abundance within 1 au from the protosun were extracted and used as input for a Monte Carlo code to model water associative adsorption using adsorption energies that resemble the forsterite [100] crystal lattice.

Results. Hydration of forsterite surfaces by water vapor adsorption could have occurred within the nebula lifetime already at a density of 10^8 cm^{-3} , with increasing surface coverage for higher water vapor densities. Full surface coverage is attained for temperatures lower than 500 K, while for hotter grain surfaces water cluster formation plays a crucial role. Between 0.5 and 10 number of Earth's oceans can arise from the agglomeration of hydrated $0.1 \mu\text{m}$ grains into an Earth-sized planet. However, if grain growth occurs dry and water vapor processes the grains afterwards, this value can decrease by two orders of magnitude.

Conclusions. This work shows that water cluster formation enhances the water surface coverage and enables a stable water layer to form at high temperature and low water vapor density conditions. Finally, surface diffusion of physisorbed water molecules shortens the timescale for reaching steady state, enabling phyllosilicate formation within the solar nebula timescale.

Key words. Solar nebula – Water adsorption – Protoplanetary disks model – Meteorites hydration – Water cluster – Monte Carlo code – Earth's water

1. Introduction

After almost 40 years of study, the origin of Earth's water is still strongly debated (Drake 2005). One hypothesis is that Earth accreted from a mixture of dry and wet primary building blocks in which water was in the form of hydrous silicates (the *wet-endogenous* scenario); another view supports dry accretion, with water delivered at a later stage during impact of hydrous asteroidal or cometary bodies (the *exogenous* scenario).

A direct evidence of aqueous alteration processes in the solar nebula is contained in Carbonaceous Chondrites (CCs). These "undifferentiated" meteorites are considered primitive Solar System objects along with Interplanetary

Dust Particles (IDPs) and cometary grains because they show solar composition (Barrat et al. 2012). Depending on the chemical and mineralogical composition and size of their parent body, several classes of CCs are defined (Weisberg et al. 2006). Among them, CI (Ivuna-like) group, CM (Mighei-like) group and CR (Renazzo-like) carbonaceous chondrites are the most hydrous varieties, with 3 to 14 wt% of water content in CM and CR, and up to 15 wt% in CI (Alexander et al. 2010). Most of the water in these chondrites is structurally bound in phyllosilicates¹ that formed during aqueous alteration of anhydrous miner-

¹ Layered silicate platelets with swelling properties (Schuttlefield et al. 2007).

als (e.g. olivine and pyroxene) very likely on the meteorites parent bodies (Brearley 2006). Recent mid-IR spectroscopy measurements revealed that the most aqueous altered samples are (–OH)-rich and almost depleted in olivine, the "dry" precursor mineral (Beck et al. 2014).

The high variability in the abundance and in the nature of these hydro-silicates in CCs indicates many levels of aqueous alteration and suggests different possible origins and evolution. Most of the models that have been developed over the last 30 years are based on the fluid flow and liquid water-rock interaction on their parent bodies: previously accreted water ice melts, the fluid flows through various mineral matrices of different permeability and reacts with the anhydrous precursor mineral finally forming the hydrated products (see review by Brearley 2006). The chemical composition of phyllosilicates forming by the flow of fluids may be controlled by the composition of the anhydrous precursor mineral and/or the composition of the aqueous solutions (Howard et al. 2011; Velbel et al. 2012).

On the other hand, hydrated silicates could have formed by direct condensation of water vapor within the terrestrial planets forming region. First models indicated that silicate hydration would be kinetically inhibited in a nebular setting (Fegley & Prinn 1989). Using a Simple Collision Theory (SCT) model and the activation energy of 8420 K (70 kJ mol^{-1}) as the amount of energy required to convert MgO into $\text{Mg}(\text{OH})_2$ (brucite) at 1 atmosphere, they estimated the formation rates of serpentine and brucite and concluded that formation of hydrous silicates takes too long to occur by nebular condensation (10^5 times the nebular life time of 10^{13} s). However, Ganguly & Bose (1995) used the same SCT approach and estimated a shorter time scale for the hydration of olivine if a lower activation energy (about 3909 K, that is 32.5 kJ mol^{-1}) is assumed in the calculation.

In the attempt to explain the presence of phyllosilicates fine-grained rims (FGRs) in the Murray CM chondrite, Ciesla et al. (2003) draw a scenario in which, holding the 8420 K of hydration energy, shock waves pass through an icy region of the nebula, the water vapor partial pressure is locally enhanced, thus increasing the collision rates of water molecules with the bare grains. Therefore, hydrated silicates can form much faster than the solar nebula life time, allowing a nebular origin of the chondrules and the phyllosilicates components as well. Woitke et al. (2017) consider phyllosilicates in thermo-chemical equilibrium, and found that below 345 K and at one bar, the dominant phyllosilicate is $\text{Mg}_3\text{Si}_2\text{O}_9\text{H}_4$ (lizardite) which replaces Mg_2SiO_4 in chemical + phase equilibrium.

Phyllosilicates can retain water when heated up to a few hundreds of degrees centigrade (Beck et al. 2014; Davies 1996) being able to preserve structural water also in the inner and warmer regions of a protoplanetary disk. Once agglomerated into planetesimals, phyllosilicates could be a potential source of water for terrestrial planets, in line with the wet-endogenous scenario.

More recent computer simulations have studied water adsorption energy, binding sites and mechanisms (associative and/or dissociative) on forsterite surfaces and demonstrated that many Earth oceans could efficiently form *in situ* under accretion disk conditions (Stimpff et al. 2006; Muralidharan et al. 2008; King et al. 2010; Asaduzzaman et al. 2013, 2015; Prigiobbe et al. 2013). However, these modeling attempts possess some major uncertainties, namely a detailed temperature-pressure structure of the

young solar nebula. In the exploratory rate-based warm surface chemistry model of Thi et al. (2018, submitted), water from the gas-phase can chemisorb on dust grain surfaces and subsequently diffuse into the silicate bulk. The phyllosilicate formation model was applied to a zero-dimensional chemical model and to a 2D protoplanetary disk model (ProDiMo) to investigate the formation of phyllosilicates in protoplanetary disks.

In this work we test the possibility of water vapor condensation on bare forsterite grains in the region of the terrestrial planets prior to their accretion into planetesimals. In the endogenous scenario, we want to quantify how much water could have been delivered to planetesimal precursors of Venus, Earth and Mars 4.5 Gyr ago. We used the astrophysical model for protoplanetary disks, ProDiMo (Woitke et al. 2009), and the Monte Carlo (MC) simulation optimized for studying accretion of ice mantles on grains (Cazaux et al. 2010, 2015), both described in sections 2.1 and 3.1. Using T Tauri disks observed in the Orion Nebula as templates, with ProDiMo we carefully build up our early solar nebula model at three time steps in the Sun's evolution. Temperature and pressure radial profiles and water vapor abundance are then extracted specifically for the midplane region close to the protosun. We use the MC simulations to calculate water adsorption rates. Surface coverages at different physical conditions were then estimated and used to quantify possible scenarios on the origin of water on terrestrial planets and meteorites.

2. Simulating the early solar nebula with ProDiMo

Over the last decades the thermo-chemical evolution of our solar nebula has been modeled with different approaches and assumptions. In some of them, the temperature and pressure gradients at different nebula stages were extrapolated from the condensation curves for actual solar system's bodies (Cameron 1995; Fegley 1999; Lewis 1974), and in others the temperature and pressure gradients are a result of simulations of protoplanetary disks with typical solar nebula parameters (Willacy et al. 1998; Makalkin & Dorofeeva 2009).

To this latter approach belongs the (1+1D) model developed by Davis (2005a,b) to study the dependency of the surface density radial distribution from the disk accretion rate. Min et al. (2011) modeled the solar nebula conditions using 3D radiative transfer to investigate how the snow line changes with evolving mass accretion rate. Hersant et al. (2001) used the (1+1D) disk structure turbulent model of (Huré & Galliano 2001) applied to the solar nebula, to extract the density and temperature profiles favorable for the D/H enrichment in LL3 meteorites and comets. Albertsson et al. (2014) combined an extended gas-grain chemical model, which accounts for high-temperature and surface reactions with multiply deuterated species, with a (1+1D) steady-state α -viscosity nebular model to obtain molecular abundances and D/H ratios for a 1 Myr old solar nebula. However, in all these models, the input parameters are not necessarily informed by typical protoplanetary disks as they are observed now in tremendous detail.

The early solar nebula disk structure presented in this work uses the protoplanetary disk modeling code ProDiMo (Woitke et al. 2009; Aresu et al. 2012). The code was developed to consistently calculate the physical, thermal and chemical structure of protoplanetary disks. It uses

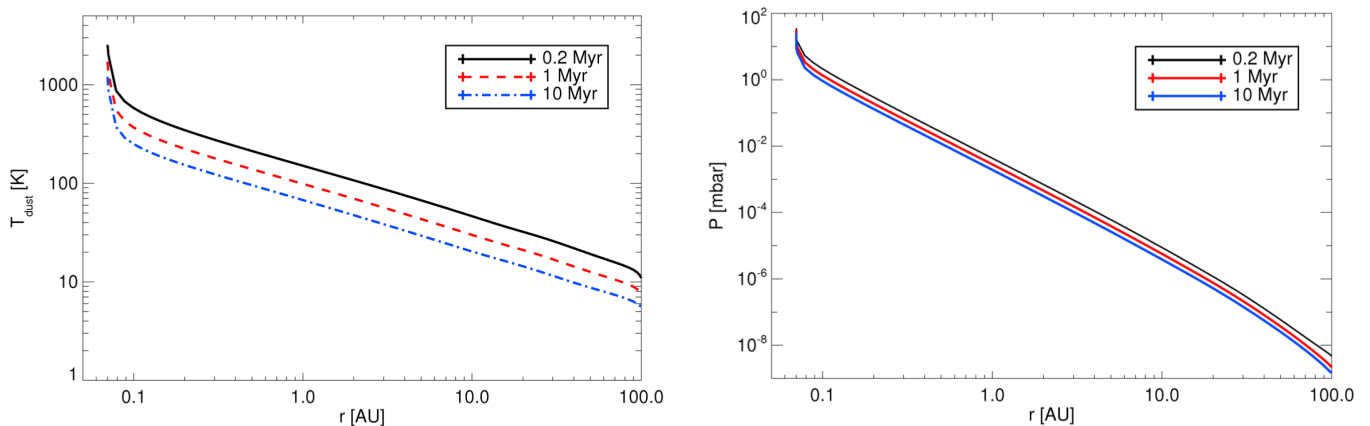


Fig. 1. Midplane ($z/r = 0.00$) dust temperature (left) and pressure (right) radial profiles extracted from ProDiMo models of the early solar nebula at three ages (0.2 Myr, 1 Myr and 10 Myr) and $0.03 M_{\odot}$ disk mass.

Table 1. List of the stellar and disk parameters

Parameters	Symbol	Value
Stellar Mass	M_*	$1 M_{\odot}$
Stellar Luminosity	L_*	11.02, 2.17, 0.46 L_{\odot}
Effective temperature	T_{eff}	4147, 4282, 4290 K
UV luminosity ^a	L_{UV}	0.01 L_{\odot}
X-ray luminosity ^a	L_{X}	$10^{30} \text{ erg s}^{-1}$
Cosmic ray ionization rate	CRI	$1.7 \times 10^{-17} \text{ s}^{-1}$
Disk mass	M_{d}	0.003, 0.03 M_{\odot}
Disk inner radius	R_{in}	0.07 au
Disk outer radius	R_{out}	100 au
Tapering-off radius	R_{tap}	50 au
Reference scale height	H_0	0.4 au
Reference radius	R_{ref}	10 au
Dust settling turbulence	α	0.1
Column density index ^a	ϵ	1.0
Dust-to-gas mass ratio ^a	$\rho_{\text{d}}/\rho_{\text{g}}$	0.01
Min. size dust grain ^a	a_{min}	$0.05 \mu\text{m}$
Max. size dust grain ^a	a_{max}	$3000 \mu\text{m}$
Dust size distr. index ^a	p	3.5
Dust composition ^a :		
Mg _{0.7} Fe _{0.3} SiO ₃		60%
amorph. carbon		15%
porosity		25%
Dust material density	ρ_{gr}	2.076 g cm^{-3}

Notes. ProDiMo input parameters used to model six early solar nebula, for two disk mass values ($0.003 M_{\odot}$ and $0.03 M_{\odot}$) at three nebular ages (0.2 Myr, 1 Myr and 10 Myr), to which the following stellar parameters (L_* and T_{eff}) correspond respectively ($11.02 L_{\odot}$, 4147 K), ($2.17 L_{\odot}$, 4282 K) and ($0.46 L_{\odot}$, 4290 K). ^(a) Standard values from Helling et al. (2014) and Woitke et al. (2009).

2D dust continuum radiative transfer, gas phase and photochemistry and a detailed thermal energy balance for the gas. ProDiMo models have been successfully applied to explain simultaneously multi-wavelength observations of dust and gas (including resolved images) in disks around young stars (see Thi et al. 2010; Woitke et al. 2011; Tilling et al.

2012; Garufi et al. 2014). The code uses now the more realistic disk dust opacities from Min et al. (2016), which can simultaneously reproduce thermal, scattering and polarization data from disks. Recently, Woitke et al. (2016) proposed a parametrized set-up for disk models that can capture enough complexity to match observations without introducing too many free parameters.

In the following, we use this parametrized set-up of ProDiMo to simulate a young solar nebula under steady-state condition around a Sun-like star at three evolutionary stages.

2.1. Physical input parameters

The study of the oxygen isotope fractionation found in meteoritic mineral inclusions revealed that the protosun probably formed in a high mass star forming region at a distance of ~ 1 parsec from an O or B star (Young et al. 2011). However, some uncertainty remains as to the cluster size (Adams 2010). Therefore, protoplanetary disks observed in the Orion Nebula (also called proplyds) are used here as templates to build our astrophysical model of the early solar nebula. The stellar and disk input parameters chosen for this work are listed in Table 1.

UV and X-ray luminosities are fixed to standard values in circumstellar disks (Woitke et al. 2016). We neglect here the presence of the external UV radiation field by the possible nearby O and B stars; its impact on the disk midplane temperatures inside ~ 1 au — the region relevant for our study of dust hydration — is negligible (Walsh et al. 2013). However, as shown by e.g. Walsh et al. (2013), Antonellini et al. (2015) and Rab et al. (2018) such enhanced external UV and X-ray radiation fields can have profound consequences for disk surface layers and the outer disk midplane which are readily observable through mid-IR and submm line emission of water and ion molecules.

Throughout the solar nebula, dust abundance and size distribution are assumed constant, with the latter following the power-law $f(a) \sim a^{-p}$, with index $p = 3.5$ (Woitke et al. 2009) and grain sizes between $a_{\text{min}} = 0.05 \mu\text{m}$ and $a_{\text{max}} = \mu\text{m}$ (see Table 1). The dust in our models is that part of solids that are accessible through observations of protoplanetary disks such as SEDs. These disks could contain already larger solids, but evidence for that is so far in-

direct from e.g. dating meteorites and putting constraints on ages of their parent asteroids in our Solar System (e.g. Amelin et al. 2005, 2006) or disk substructure as revealed by SPHERE and ALMA images (e.g. Pérez et al. 2014; Benisty et al. 2015) which could indicate planetary mass companions (de Juan Ovelar et al. 2016).

The comparison between the disk mass distribution of the Submillimeter Array (SMA) survey of 55 proplyds in Orion and similarly-aged disks in the low mass star forming regions Taurus and Ophiuchus shows that the Orion disk distribution is statistically different from the other two. The number of disks per logarithmic mass bin is approximately constant for masses $0.004 - 0.04 M_{\odot}$ in all three regions, but Orion lacks disks more massive than $0.04 M_{\odot}$ (Mann & Williams 2012). Accordingly, $0.03 M_{\odot}$ and $0.003 M_{\odot}$ were chosen as representative values for the disk mass of our early solar nebula.

Most of the previous solar nebula models are based on the Hayashi Minimum-Mass-Solar Nebula representation (MMSN), where the local surface density is given by the mass of each planet spread on an appropriate annular area. In that case the surface density scales as a power law with index equal to $-3/2$ (Weidenschilling 1977; Hayashi 1981). The surface density profile in our work is assumed to be a power law

$$\Sigma(r) = \Sigma_0 r^{-\epsilon} e^{(-r/R_{\text{tap}})}, \quad (1)$$

with index ϵ equal to 1, less steep than the MMSN but in agreement with observations of proplyds in Orion Nebula (Mann & Williams 2010). The exponential factor causes a tapering-off for the outer edge, meaning that at R_{tap} the disk surface density profile starts an exponential cut-off and most of the disk mass will be contained therein.

The disk size was extracted from the disk diameter distribution histogram made for the total sample of 149 proplyds observed in the Trapezium cluster of Orion Nebula with the HST (Vicente & Alves 2005) and the SMA (Mann & Williams 2010). It indicates that 75 to 80% of disks have diameters smaller than 150 au and 40% of those have disk radii larger than 50 au. Hence, we picked a radius of 50 au as taper radius for our solar nebula.

In ProDiMo, the vertical disk structure is fully parametrized. Given a scale height, H_0 , at a reference radius, R_{ref} , the scale height of the disk is given as

$$H = H_0 (r/R_{\text{ref}})^{1.1}. \quad (2)$$

This work studies a disk at the end of the cloud core collapse, corresponding to a protostar + disk system older than 10^5 years. Three evolutionary stages are considered here: 0.2 Myr, 1 Myr and 10 Myr. The dust temperature profile is given by solving the 2D dust continuum radiative transfer equation. The luminosity and effective temperature of our protosun were picked from the evolutionary tracks that the Grenoble stellar evolution code for pre-main sequence stars (Siess et al. 2000) gives for a $1 M_{\odot}$ star of solar metallicity ($Z = 0.02$) at three evolutionary ages: 0.2 Myr, 1 Myr and 10 Myr. We find stellar luminosity (L_*) and effective temperature (T_{eff}) pairs respectively of ($11.02 L_{\odot}$, 4147 K), ($2.17 L_{\odot}$, 4282 K) and ($0.46 L_{\odot}$, 4290 K). We use here passive disk models, i.e. we neglect the extra heating in the inner disk midplane regions that stems from accretion. Even though we observe mass accretion through e.g. studies of emission lines, the

underlying momentum transport and how the mass accretion occurs is less clear than it was in the past; this is due to simulations now including non-ideal MHD effects (e.g. Lesur et al. 2014) and recent ALMA studies putting strong limits on levels of turbulence, both indicating that the disks are in large parts more laminar than originally thought (e.g. Flaherty et al. 2018).

2.2. Temperature and pressure disk radial profiles

The dust temperature (T_{dust}) and pressure radial profiles at the disk midplane ($z/r = 0.00$) were extracted from six early solar nebula models: two disk mass limits ($0.003 M_{\odot}$ and $0.03 M_{\odot}$) at three nebular ages (0.2 Myr, 1 Myr and 10 Myr). In the following figures, only the values for the highest disk mass are shown for simplicity.

The youngest disk at the inner radius (fixed to 0.07 au) is hotter than the other two older models (Fig. 1, left). The main difference in the three ages is the stellar luminosity, which determines the main heating source in the innermost regions close to the protosun. The dust inner-rim is heated by the stellar radiation, which is stronger for the youngest protosun. The maximum temperature far exceeds the dust condensation temperature. It ranges from about 2700 K for the 0.2 Myr old disk (black curve) to 1770 K at 1 Myr (red curve) and finally to about 1210 K for the 10 Myr model (blue curve). Here the inner radius was not adapted to a unified dust condensation temperature, since our primary goal is not to capture the intricate details of the inner rim of the disk. Our study focuses on the midplane region where T_{dust} ranges between 300 K and 600 K (Sec. 3.1). There are no differences in the midplane temperature profiles for the two disk masses considered.

The radial pressure profile (right side of Fig. 1) follows the trend of the dust temperature. Indeed, from Eq. (1) and Eq. (2), it is clear that the column density is fixed and the mass is distributed according to our prescription, so the volume density is not changing with age in our models. For disks with mass $0.03 M_{\odot}$, the pressure is simply one order of magnitude higher than for $0.003 M_{\odot}$ disks. This is true for the very optically thick part of the midplane.

Figure 2 offers an overview of the state-of-the-art of previous solar nebula simulations in terms of temperature and pressure values at three representative distances from the protosun. A big discrepancy between our temperature values and the ones given in Lewis (1974), Cameron (1995) and Willacy et al. (1998) simulations exists throughout the disk. At 0.1 au, our youngest nebula (0.2 Myr old) is two times colder than Willacy et al. (1998) nebula and a factor of 13 colder than Lewis (1974) model. At 1 au the gap decreases to a factor of four and at 10 au our disk becomes two times colder indicating a very different slope of $T(r)$. For the pressure, there is an overall good agreement, except for the values in Lewis (1974) model which are two orders of magnitude larger than ours. Lewis (1974) and Cameron (1995) models, based on the condensation curves of the actual composition of the solar system's bodies, predict an adiabatic temperature-pressure dependency, far from our ProDiMo disks in thermal equilibrium. The 1D vertical structure model of a viscously heated disk ($\alpha = 0.01$, $\dot{M} = 10^{-7} M_{\odot} \text{ yr}^{-1}$, $R_{\text{disk}} = [0.1 - 100] \text{ au}$) described by Willacy et al. (1998) is slightly closer to ours. However, differences in input parameters likely cause the tempera-

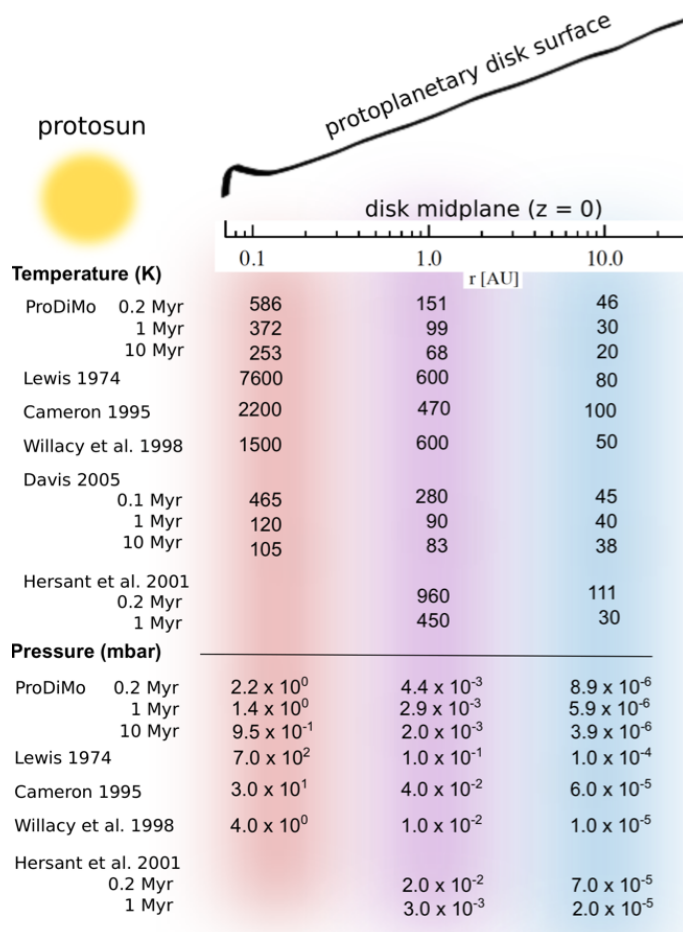


Fig. 2. Overview of the thermal and pressure profiles of our early solar nebula model compared to previous simulations. ProDiMo values are for a $0.03 M_{\odot}$ disk. Values from Lewis (1974), Cameron (1995) and Willacy et al. (1998) used in Fig. 1 of Fegley (1999) are extrapolated to 0.1 au. ($P-T$) values of Hersant et al. (2001) and Davis (2005a) are extracted from their figures.

ture differences. Differences are also seen for the ($P - T$) values taken from the solar nebula simulation of Hersant et al. (2001). The model was calculated using $\alpha = 0.009$, $M_{\text{disk}} = 0.3 M_{\odot}$ and it results in $R_{\text{out}} = 42$ and 32 au respectively for 1 and 0.2 Myr old disk. A good agreement exists between our temperature values and those of Davis (2005a), who implemented a β -prescription for the viscous heating in the 2D disk model from Dullemond et al. (2002).

In an active disk the viscous heating of the gas by accretion of material from the disk towards the protosun increases the dust temperature in the midplane by thermal accommodation with the gas. The effect of viscous heating is not captured in our ProDiMo models of a passive disk, in which the column density is fixed, the mass is distributed according to our prescription and dust and gas are thermally coupled in the midplane. This can explain the large deviations between the accretion models discussed earlier and the set of simulations studied in this work.

3. Monte Carlo simulation of water adsorption on forsterite surface

In order to test the wet endogenous scenario, Stimpfl et al. (2004) quantified the amount of water molecules adsorbed on grain surfaces. A grid of 10 000 sites, considered to mimic the dust surface, could interact with an infinite reservoir of water molecules, where a maximum of one monolayer is allowed for physisorption with the bare surface (adsorption energy about 600 K, corresponding to 5 kJ mol^{-1}). They consider the increase of binding energy due to the cooperative behavior of neighboring water molecules for the formation of clusters. At steady state only 0.25% of Earth's ocean could accrete at 1000 K and 3% of it at 500 K. Stimpfl et al. (2006) considered an atomistic approach to investigate water adsorption kinetics on the [100] and [010] forsterite crystal planes. The calculation of the surface energy potential distribution showed that the forsterite surface is mostly hydrophobic since the low coordinated surface Mg atoms are the only "attractive" binding sites.

Based on this work, Muralidharan et al. (2008) studied the mechanisms of adsorption of water onto forsterite surfaces combining an energy minimization technique with a kinetic Monte Carlo simulation. This study showed that at 700 K and 10^{-5} mbar of water partial pressure a single layer coverage of $15 \text{ H}_2\text{O nm}^{-2}$ forms for the [100] crystal lattice, while the [010] orientation is less reactive (about $1 \text{ H}_2\text{O nm}^{-2}$).

King et al. (2010) investigated the chemisorption of water molecules with adsorption energies as high as 38 511.5 K ($320.2 \text{ kJ mol}^{-1}$) versus 19 243.7 K ($160.0 \text{ kJ mol}^{-1}$) of Stimpfl et al. (2006) for the stoichiometric [100] lattice. Their calculation also showed that defective [100] and [010] surfaces are more reactive and hence favorable to H_2O adsorption than the stoichiometric ones, playing a crucial role at lower water partial pressures ($\sim 10^{-8}$ bar) and high temperatures (~ 1500 K). Subsequent numerical calculations extended the investigation from vacuum to ambient conditions (Prigobbe et al. 2013) and included different crystal orientations and adsorption sites of the mineral (Asaduzzaman et al. 2013, 2015). However, a detailed temperature-pressure structure of the young solar nebula is needed as a benchmark to evaluate the wider astrophysical implications.

In this work we have investigated water adsorption by means of a Monte Carlo (MC) numerical code developed by Cazaux et al. (2010, 2015). With our simulations we address the following questions:

1. How much water molecules can adsorb on dust surfaces according to the ($T, n_{\text{H}_2\text{O}}$) parameters space typical from morphological (thermal and aqueous) alterations of the grains?
2. Which surface mechanisms and properties (adsorption, evaporation, binding energy, cluster formation, etc.) compete for the formation of the first water layer?
3. Where in the nebula can water vapor condensation efficiently hydrate meteoritic and asteroidal mineral components?
4. Is this a possible scenario to explain the presence of water on Earth?

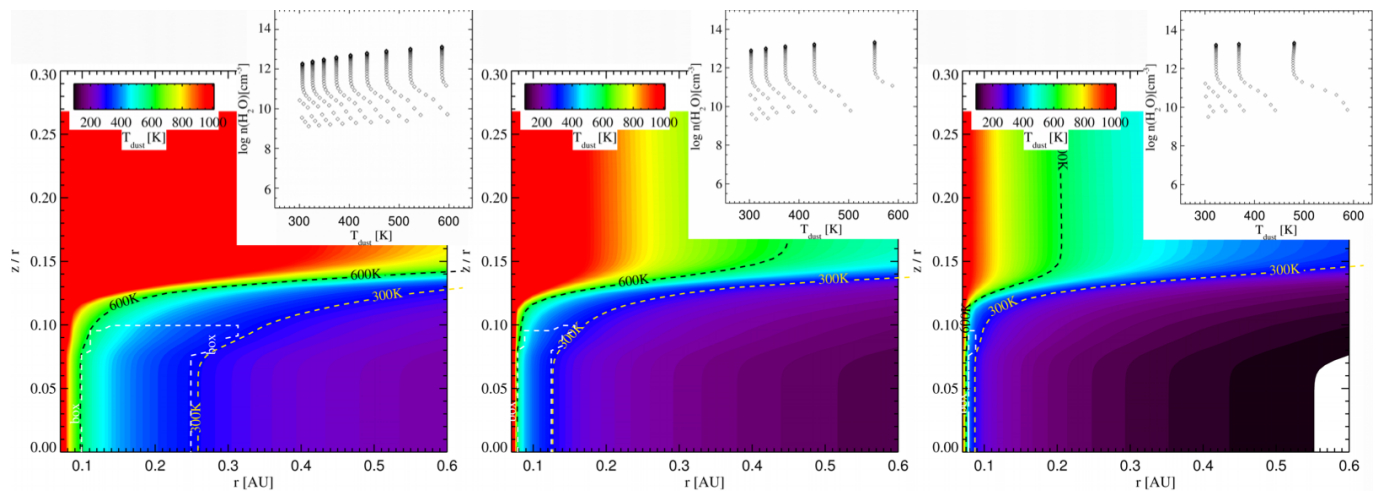


Fig. 3. From left to right: dust temperature structure $T_{\text{dust}}(r, z/r)$ from ProDiMo models for a $0.03 M_{\odot}$ disk respectively 0.2 Myr, 1 Myr and 10 Myr old. White dashed lines identify the $(T, n_{\text{H}_2\text{O}})$ parameters space called *box* and analyzed in this work. The insert figures show the logarithmic scale of water vapor density $n_{\text{H}_2\text{O}}$ as a function of T_{dust} . Within the *box* it ranges between 10^9 and 10^{13} cm^{-3} .

3.1. Input parameters

Our study focuses on the hydration of forsterite surface grains by water vapor condensation in the habitable zone. We have defined a region in the disk midplane ($z/r < 0.1$) where the gas and dust temperatures are coupled and referred to as the surface temperature in our MC models ($T_{\text{gas}} = T_{\text{dust}} = T$) and range from 300 K up to 600 K. This *box* changes location in the nebula, moving inward or outward and/or shrinking depending on the nebula’s age, hence stellar luminosity (see Fig. 3). The H_2O vapor density as function of temperature (inserts of Fig. 3), which correspond to the conditions in the box, was extracted from each ProDiMo model. Three values were here used as input parameters in the MC simulation within the range $[10^8 - 10^{13}] \text{ cm}^{-3}$ (see Table 2).

In our MC simulation the [100] forsterite crystal lattice is considered and consists of a grid composed by 20×20 sites with a total surface area of 27.04 nm^2 . According to previous DFT calculations (Stimpfl et al. 2006), the unit cell shows four possible binding sites corresponding to Mg cations, three of which are closer to the surface and easily accessible to water molecules. The highest binding sites of about 19240 K (160 kJ mol^{-1}) represent 45% of the total number of sites, while binding sites with energies around 15640 and 8420 K (130 and 70 kJ mol^{-1} , respectively) represent 15 and 30% of the total number of sites. We created a step-like function to reproduce the surface energy distribution of a [100] crystal lattice by using three Maxwell-Boltzmann distributions with central energies at 8420 K, 15640 K and 19240 K, listed in Table 2.

Each water molecule is sent randomly onto the surface and its track is recorded from the moment of its adsorption, through surface diffusion up to its eventual desorption. In this work we focus on the formation of the first monolayer, preliminary stage for water diffusion into the bulk (Thi et al. 2018, submitted). The adsorption of water molecules from the gas phase occurs at a rate

$$R_{\text{ads}} = n_{\text{H}_2\text{O}} \nu_{\text{H}_2\text{O}} \sigma S \quad \text{s}^{-1}, \quad (3)$$

which depends on the density of water molecules $n_{\text{H}_2\text{O}}$, their thermal velocity $\nu_{\text{H}_2\text{O}} \sim 0.43\sqrt{T_{\text{gas}}/100} \text{ km s}^{-1}$, the cross

Table 2. List of the input parameters for the Monte Carlo simulation

Parameter	This work	Comparison work
$n_{\text{H}_2\text{O}}$ (cm^{-3})	6(8), 6(10), 6(12)	1(11) ^a
T (K)	300 – 800	700 – 1200 ^a 1000 – 1500 ^e
E_{ads} (K)	8420 (55%)	
(100)	19240 (15%) 15640 (30%)	19240.4 ^c , 19240 ^b 16120 ^a , 15132.4 ^d
N_{sites}	400	32 ^a
$N_{\text{grid cells}}$	400	3924 ^a , 10000 ^e
cell size (nm^2)	0.06700	0.00062 ^a

References. (a) Muralidharan et al. (2008); (b) Stimpfl et al. (2006); (c) King et al. (2010); (d) Prigiobbe et al. (2013); (e) Stimpfl et al. (2004).

Notes. The (..) notation indicates the power of 10.

section σ of the dust surface, which scales with the size of the grid (here $6.76 \times N_{\text{sites}}^2 \text{ \AA}^2$) and the sticking coefficient S (assumed equal to 1).

If a water molecule lands in a site surrounded by neighboring H_2O , its binding energy increases linearly with the number of neighboring molecules (Cuppen & Herbst 2007) as 0.22 eV per hydrogen bond (Dartois et al. 2013) until a maximum of 0.88 eV is reached when a water molecule is surrounded by four neighbors. By increasing the binding energies of water molecules as they are surrounded by other water molecules, we are including the formation of water clusters in our model, and can address the contribution of such clusters for the formation of the first water layer.

We also include surface diffusion of water molecules. Once landed on the grid, the water molecules can also move from one site to another with a diffusion rate

$$R_{\text{diff}} = \nu \exp\left[-0.4 \times \frac{n_{\text{nb}} E_b}{T}\right] \quad \text{s}^{-1},$$

where ν is the vibrational frequency of a water molecule in its site, that is 10^{12} s^{-1} , E_b is the energy of a single

hydrogen bond, and n_{nb} the number of neighbors. The activation energy for diffusion is 40% of the binding energy, as in Cazaux et al. (2015); hence, it depends on the binding site and number of neighboring water molecules.

Once adsorbed on the surface, water molecules can sublimate back into the gas phase. The desorption rate depends on the binding energy of the water molecules and is therefore directly dependent on the number of neighbors n_{nb} . The desorption rate of one water molecule with n_{nb} neighbors can therefore be written as

$$R_{\text{des}} = \nu \exp\left(-\frac{n_{\text{nb}}E_b}{T}\right) \quad \text{s}^{-1}.$$

While desorption rates increase exponentially with the surface temperature, accretion rates increase linearly with the density of water molecules. The coverage of water molecules on dust surfaces is governed by these two competing mechanisms. In the next section, we address the kinetics of forsterite hydration.

3.2. Results from Monte Carlo simulation

We have performed several simulations with equal grid properties at temperatures and water vapor densities indicated in Table 2. Our motivation is to study how much water can be accreted onto dust grains in the parameter space ($T, n_{\text{H}_2\text{O}}$) that defines the region between 0.07–0.3 au from the protostar where the raw material for terrestrial planets may have experienced morphological (thermal and aqueous) alterations.

In Figure 4, adsorption rates of water vapor molecules onto the forsterite [100] crystal lattice are shown for various surface temperatures ($T_{\text{gas}} = T_{\text{dust}}$) and water vapor densities of $6 \times 10^8 \text{ cm}^{-3}$ (top), $6 \times 10^{10} \text{ cm}^{-3}$ (middle) and $6 \times 10^{12} \text{ cm}^{-3}$ (bottom). For the lowest water vapor density considered, at 300 K the [100] crystal surface is fully covered by one monolayer which represents $15 \text{ H}_2\text{O nm}^{-2}$, at 400 K about 90% of the surface is hydrated; at a temperature between 500 K and 600 K the surface coverage drops to about 30% of the total surface area and at 800 K no water molecules stick to the surface. Upon exposure to the intermediate water density (see Fig. 4 middle plot) the coverage at equilibrium increases for each considered temperature. At the highest water vapor density (see Fig. 4 bottom plot) at 800 K one third of the forsterite grain can retain water on its surface. The equilibrium for the formation of one monolayer is rapidly achieved within 100 s at the lowest vapor density, within 10 s for the intermediate density value and less than 0.1 s for the highest vapor density considered.

The average surface coverage at equilibrium was calculated and plotted as a function of temperature (Fig. 5 left panel) and density (Fig. 5 right panel). This figure illustrates the competition between accretion and evaporation, and the formation of clusters. While at low temperatures the surface is fully covered by water molecules, this coverage decreases at different paces depending on the accretion rates (densities). The higher the density, the higher the accretion rates and the ability to form water clusters (and therefore increasing the binding energies).

The decrease of surface coverage for increasing temperatures is not linear, but reflects the step-like function used to describe the three different types of binding sites with

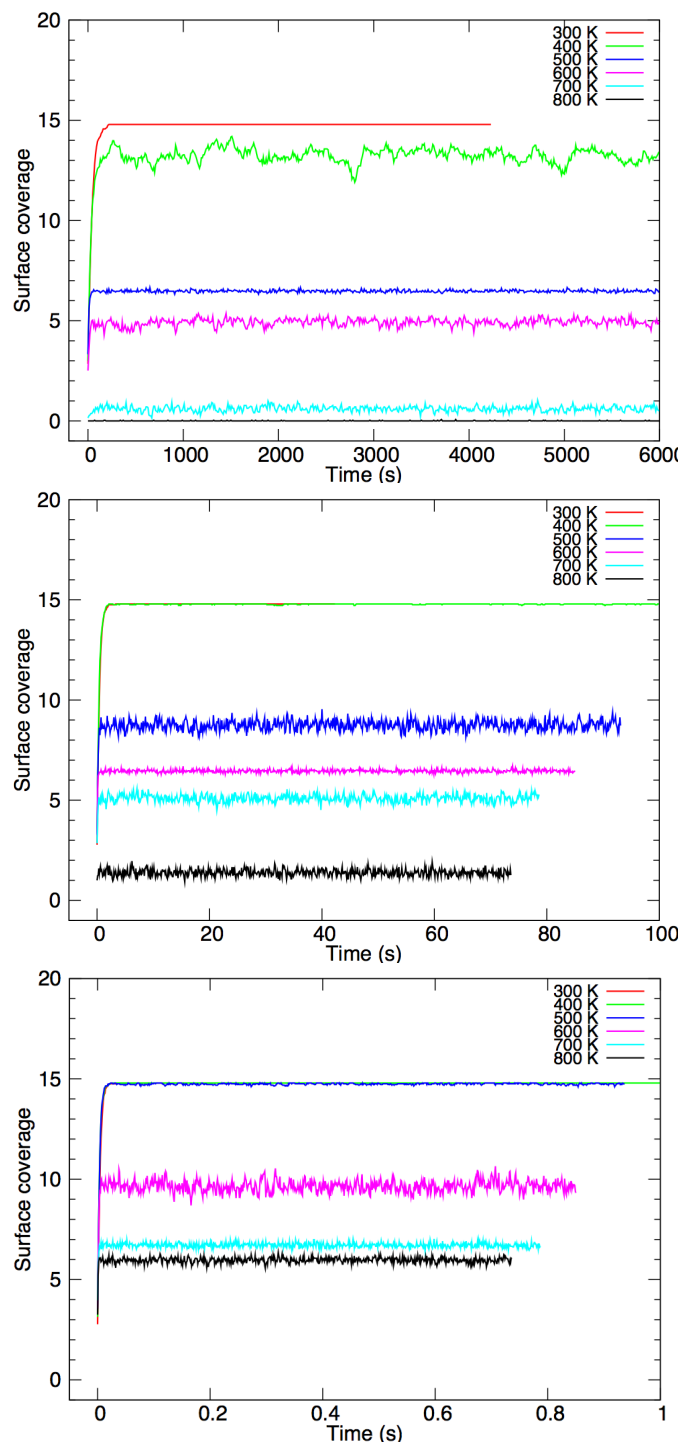


Fig. 4. Surface coverage ($\text{H}_2\text{O nm}^{-2}$) as a function of time (s) at three water vapor densities: 6×10^8 (top), 6×10^{10} (middle) and 6×10^{12} (bottom) cm^{-3} and temperatures between [300–800] K (see the legend). Except for 300 K, at each temperature the adsorption rate increases with the water vapor density and equilibrium is reached within fractions of a second for a density of $6 \times 10^{12} \text{ cm}^{-3}$.

different binding energies (see Table 2). This distribution of binding sites and the cluster effect also cause the surface coverage to decrease to zero smoothly when approaching 700 K and 800 K. For an increasing $n_{\text{H}_2\text{O}}$, the surface coverage increases also not linearly, as shown in Fig. 5 right panel. This is more visible for higher temperatures and re-

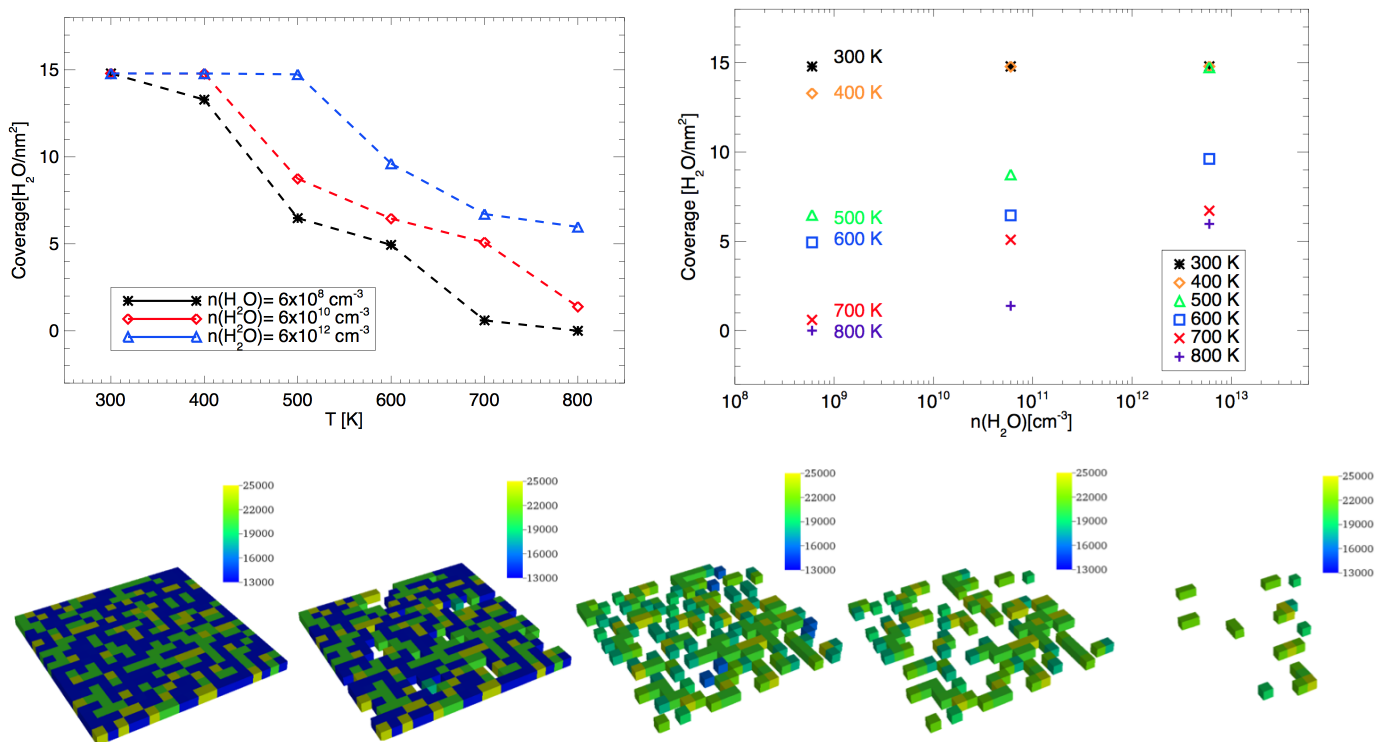


Fig. 5. Top: surface coverage ($\text{H}_2\text{O nm}^{-2}$) as a function of temperature (K) (left) and water vapor density (cm^{-3}) (right). Each data point is the average $\pm\sigma$ of the coverage values at equilibrium (see Fig. 4). Left: dashed lines are used here to link each point and emphasize the step-like decrease of the surface coverage with the temperature. Bottom: simulated [100] forsterite surface grids at $6 \times 10^8 \text{ cm}^{-3}$ and $T = [300 - 700] \text{ K}$ (from left to right). The color scale indicates the adsorption energy of the occupied sites in the range between 13 000 K (blue) and 25 000 K (yellow).

flects the competition between desorption and adsorption of water molecules which are allowed to cluster around an occupied site.

In our MC simulations two important surface processes were implemented: surface diffusion and water cluster formation. The latter helps water molecules to increase their binding energies as other adsorbed molecules, present in neighboring sites, will add energies to the binding through H-bonds. The effect can be seen in the lower panel of Fig. 5, where at equal water vapor density, molecules resist thermal desorption by forming a "cluster" around an occupied site thus increasing their adsorption energy. As claimed in de Leeuw et al. (2000) and Stimpfl et al. (2006), this cooperative behavior increases the chances for more water to adsorb and to remain on the surface, in particular at high temperatures.

3.3. Discussion of MC simulations

In case of a gas rich in water vapor, molecular adsorption onto silicate grains would be an efficient hydration mechanism over a wide temperature range within planetary accretion time-scales.

Our results deviate somewhat from previous works. For instance, at 700 K and $6 \times 10^{10} \text{ H}_2\text{O cm}^{-3}$, similar physical parameters used by Muralidharan et al. (2008), our simulation shows that only 30% of the [100] forsterite surface is occupied by water molecules, while Muralidharan et al. (2008) obtained full surface coverage. Our equilibrium time scales are three orders of magnitude smaller than the one

obtained in Muralidharan et al. (2008) simulations (within 20 000 s at all temperatures in the range [700 – 1200] K), which is very short compared to the nebula lifetime of millions of years.

Finally, in our work the surface coverage decreases in steps with the temperature, in contrast with the results of Muralidharan et al. (2008), where an exponential trend was found for the temperature range [700 – 1200] K. These discrepancies can be due to differences between the two models and input parameters. Adsorption and a "box" of gas molecules in the random-walk regime with equal mean free path and collision frequency to the [100] forsterite surface are treated in the same way in this work and in Muralidharan et al. (2008). In Muralidharan et al. (2008), the surface potential is detailed finely using a grid sub-sampled in 3924 cells of area 0.062 \AA^2 compared to the 400 sites of 6.76 \AA^2 for our model surface. This can explain the smooth, exponential decrease of the surface coverage with the temperature versus the step-like, non-linear trend in our simulations. However, our temperature range overlaps with theirs only for two values. Besides, we allow the water molecules to scan the surface upon collision and, by lateral diffusion, to find the favorable binding site. This can explain why the time spent for the system to reach equilibrium is a factor of 1000 shorter than in Muralidharan et al. (2008), where a simple collision theory is considered.

To further understand the reason for the differences, we have investigated different surface potential energy distributions (Appendix B), reproducing the energy potential in Stimpfl et al. (2006) and used in Muralidharan et al.

(2008). Again, at 700 K and $6 \times 10^{10} \text{ H}_2\text{O cm}^{-3}$ no full coverage was attained contrary to the results from Muralidharan et al. (2008). The cause of this discrepancy can depend on an oversampling of the surface sites which can affect the energy distribution.

4. Solar nebula implications

Several near- and mid-IR observations (Salyk et al. 2008; Carr & Najita 2008; Pontoppidan et al. 2010; Carr & Najita 2011; Riviere-Marichalar et al. 2012) have revealed the presence of warm water vapor (300 – 800 K) in the habitable planet-forming region (within three astronomical units) in T Tauri circumstellar disks. Embedded in this environment, small micron-sized silicate dust grains have also been observed from their signatures at 10 μm and 18 μm (e.g. Kessler-Silacci et al. 2006). Shape, intensity and exact wavelength of these spectral features are indicative of the dust morphology (crystalline or amorphous), mineralogy (i.e. forsterite, enstatite, etc.) and size properties (see for example Jäger et al. 2003; Chiang 2004; Bouwman et al. 2008).

Despite the long lasting debate on which mechanisms contributed to the water content on rocky planets of our Solar System (exogenous vs. endogenous), our work shows that water gas-solid interaction can lead to hydration of the pristine forsterite surface under nebula conditions within its lifetime. In the following, the surface coverages obtained from our MC simulations are discussed in the context of the Earth mantle water and oceans, and compared to the amount of hydrated silicates found in meteorites and observed on asteroids.

It is clear that our approach has its limitations as we neglect several processes that affect both the global and local grain size distribution in the nebula. Grain growth (and destruction), vertical settling and radial migration are processes that act in young disks as they are evolving into planetary systems, see e.g. Birnstiel et al. (2016) for a recent review. Pinte et al. (2016) show that ALMA images of the young T Tauri disk around HL Tau indicate the presence of large mm-sized grains that have settled efficiently to the midplane. On the other hand, Kruijer et al. (2014) find that the parent bodies of various types of iron meteorites likely accreted within 0.1-0.3 Myr after CAIs, thus providing support to the possibility that large bodies could already exist also in protoplanetary disks with ages of 1-3 Myr. In that context, the assumptions made below of either single small grain size or an observed homogeneous grain size distribution throughout the inner disk can only be limiting cases and more detailed studies are required in the future to combine the results from water adsorption with detailed dust evolutionary models of the inner disk.

4.1. Water content on Earth

The oceans are not the only water reservoir of our planet. Adding together the water contributions of the hydrosphere ($1.6 \times 10^{21} \text{ kg}$), the exosphere including the crust ($1.9 \times 10^{21} \text{ kg}$) and the mantle (between $0.3\text{--}2.5 \times 10^{21} \text{ kg}$) and normalizing by the mass of the Bulk Silicate Earth (BSE = mantle + crust, $4.05 \times 10^{24} \text{ kg}$), the total water budget ranges between 0.05 – 0.11 wt%. The Earth is currently 5–50 times dryer than the CV and CO, the two driest classes of C-chondrites (Mottl et al. 2007). Nevertheless, the

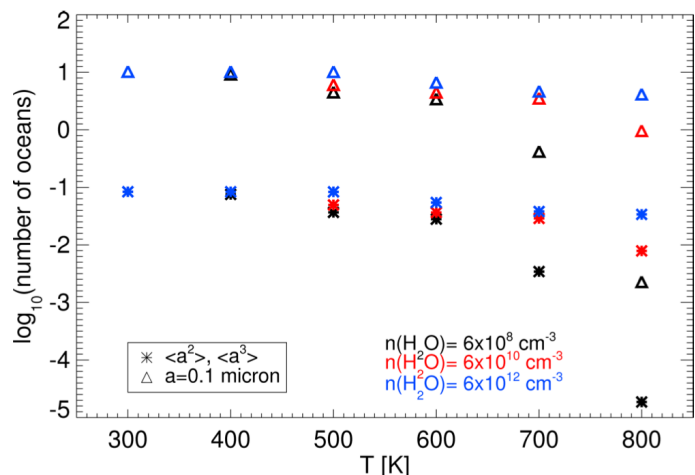


Fig. 6. The conversion of the surface coverages (Fig. 5) into number of Earth’s oceans as a function of the temperature in the range [300 – 800] K and for the three water density values $6 \times 10^8 \text{ cm}^{-3}$ (black), $6 \times 10^{10} \text{ cm}^{-3}$ (red) and $6 \times 10^{12} \text{ cm}^{-3}$ (blue). The calculation is done considering spherical dust grains of 0.1 μm average radius (Δ) and the second, $\langle a^2 \rangle$, and third moments, $\langle a^3 \rangle$, ($*$) derived from the grain size distribution.

wet bodies that collided to form our protoplanet must have possessed a larger amount of water than the actual Earth’s abundance to account for the loss of such volatile species by impact degassing.

We have estimated the Ocean Equivalent Water (OEW) by combining our knowledge of the Earth’s radius ($R_{\oplus} = 6.371 \times 10^6 \text{ m}$) and the total oceans mass ($1.4 \times 10^{24} \text{ g}$) together with the surface coverage data, here called θ ($\text{H}_2\text{O nm}^{-2}$), obtained from our MC models (see Sec 3.2). The water mass (g) adsorbed onto a spherical grain with radius a and surface area $4\pi a^2$ is

$$M_{\text{H}_2\text{O}} = 4\pi a^2 m_{\text{H}_2\text{O}} \theta, \quad (4)$$

where $m_{\text{H}_2\text{O}}$ is the water molecular mass. The number of grains equivalent to the Earth’s volume is

$$N_{gr} = \frac{R_{\oplus}^3}{a^3}. \quad (5)$$

Multiplying N_{gr} by $M_{\text{H}_2\text{O}}$ and normalizing for the oceans mass, we obtain the number of oceans that could originate from the agglomeration of N_{gr} forsterite dust grains previously hydrated by water vapor condensation.

In Figure 6, the results are plotted as a function of temperature in the range [300 – 800] K, for the three water vapor densities studied in this work, $6 \times 10^8 \text{ cm}^{-3}$ (black), $6 \times 10^{10} \text{ cm}^{-3}$ (red) and $6 \times 10^{12} \text{ cm}^{-3}$ (blue). Two sets of calculations are shown: One where we assume that the dust grains are all spheres of 0.1 μm radius (see Δ symbol in Fig. 6). A second one, where hydration occurs on grains which have previously agglomerated into larger bodies according to the power-law size distribution described in Section 2.1. These two scenarii present the extremes of assuming that grains can retain their water during the agglomeration process and grains only starting to take up water after the first agglomeration phase.

In the first scenario (see Δ symbol in Fig. 6), about 10 Earth oceans could be delivered by nebular adsorption of water molecules at 300 K and 400 K for the three densities

considered. For the lowest density value (black triangle in Fig. 6), 4.5, 3.5, 0.5 and no Earth oceans can form from water vapor condensation respectively at 500 K, 600 K, 700 K and 800 K. The number of oceans scales linearly with the surface coverage θ (see Eq. 4), which increases with the density (see Fig. 5 and Sec. 3.2). Therefore, the Earth can still inherit between one and four oceans from the agglomeration of wet 0.1 μm sized grains upon exposure at 800 K to water molecules at densities of $6 \times 10^{10} \text{ cm}^{-3}$ (red triangle) and $6 \times 10^{12} \text{ cm}^{-3}$ (blue triangle), respectively.

Assumed that the [100] surface constitutes about 44% of the surface area of a perfect forsterite crystal, for a water density of 10^{11} cm^{-3} Muralidharan et al. (2008) obtained between eight and four Earth oceans at respectively 700 K and 800 K, which are a factor of five to nine larger than our results. In a later work, Asaduzzaman et al. (2015) showed the trend of the OEW as a function of grain size for different coverage and at 900 K and 10^3 bar of water pressure (likely Earth forming condition).

Considering that 65% of the Earth's mantle is olivine mineral, agglomeration of 0.1 μm grains would account for about five and two OEW in the Earth's mantle, respectively for full or partial coverage (42% of the total surface area). This occurs with most of the $(T, n_{\text{H}_2\text{O}})$ pairs we considered in our models.

In Stimpfl et al. (2004), Monte Carlo simulations are used to evaluate the coverage of water on a substrate on a grid of 10 000 cells. These authors find that the adsorbed water potentially stored in the dust corresponds to about three times the Earth's oceanic + atmospheric + crustal water (OAC) and about 1.5 times the Earth's OAC + mantle water. According to the latest Earth's water estimation reported by Genda (2016), roughly four ocean masses are needed to account for the "surface" and mantle water. Our results demonstrate that during the early solar nebula at a distance of 0.07 – 0.3 au from the protosun and with the parameters space $(T, n_{\text{H}_2\text{O}})$ described earlier, 0.1 μm dust grains are subject to an intense aqueous alteration. By the same mechanisms that transport processed materials in- and outwards in the disk (Gail 2004; Boss 2004; Nuth et al. 2005), these wet silicates would eventually reach the terrestrial planets feeding zone (within one astronomical unit) and there supply enough water for oceans to rise.

In our ProDiMo models, the grain size distribution holds for the entire disk with the size ranging between 0.05 and 3000 μm (see Table 1). However, dust settling vertically to the midplane changes the second and third moments of the distribution. Accordingly, in Equations 4 and 5 we chose to use respectively the second and third moments of the grain size distribution (see Sec. 2.1), which are $\langle a^2 \rangle = 1.245 \times 10^{-10} \text{ cm}^2$ and $\langle a^3 \rangle = 1.525 \times 10^{-13} \text{ cm}^3$. The number of Earth oceans thus obtained are two order of magnitudes smaller than in the previous case (see * symbol in Fig. 6). In particular, between 3.5% to 8% of an ocean of water can accrete at 500 K and between 0.5% and 4% at 700 K. These results are close to the ones of Stimpfl et al. (2004), where 1% and 3% of one Earth's ocean could accrete at 700 K and 500 K respectively (see Drake 2005).

Hence, the contribution to the water content on habitable planets provided by hydrated silicates varies with the size distribution of the mineral grains: At a very early stage of our solar nebula, when grains were ISM-like, Earth could potentially inherit an amount of water equal to 10 oceans. At a late stage in the disk evolution, when dust

grains grow, water vapor condensation can contribute to less than 1% of an Earth ocean. This is a lower limit of the amount of water that can be incorporated into the grain due to the assumptions of this work. Only a single layer of water molecules was allowed to form onto a defect-free crystalline silicate surface. It was ignored that hydration is enhanced when defects are present and amorphous silicates are considered instead (Yamamoto & Tachibana 2016). Finally, we have neglected bulk diffusion into the core of the silicate grain, which has been recently shown to efficiently occur at temperatures as high as 700 K in the inner regions of a protoplanetary disk (Thi et al. 2018, submitted). All these factors can significantly enhance the amount of phyllosilicates that can form.

4.2. Phyllosilicates in asteroids

For a simple estimate of the fraction of phyllosilicates in asteroids under the scenario of hydration by water vapor, we assess which fraction of the precursor grains could be turned into phyllosilicates through surface reactions. The second moment of the grain size distribution $\langle a^2 \rangle = 1.245 \times 10^{-10} \text{ cm}^2$ provides the average surface of a grain. With a density of surface sites of $N_{\text{sites}} = 1.5 \times 10^{15} \text{ cm}^{-2}$, we find a total of 2.35×10^6 surface sites. The dust to gas mass ratio is

$$\frac{M_d}{M_H} = \frac{n_d \cdot 4\pi \langle a^3 \rangle \rho_{\text{gr}}}{n_{\langle H \rangle} \mu m_H} = 0.01, \quad (6)$$

where M_d is the mass of dust, M_H the mass of the gas (hydrogen gas), n_d the volume density of dust, ρ_{gr} the mass density of dust grains, which is 2.076 g cm^{-3} , μ is the mean molecular weight of the gas, (2.4 for H_2 gas), $n_{\langle H \rangle}$ is the total hydrogen number density in the gas and m_H the mass of hydrogen ($1.67 \times 10^{-24} \text{ g}$). The volume density of dust grain can then be written as

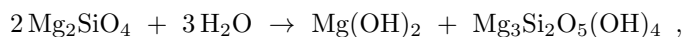
$$n_d = \frac{3 \cdot 0.01 \mu m_H n_{\langle H \rangle}}{4 \pi \langle a^3 \rangle \rho_{\text{gr}}} \quad (7)$$

with the third moment of the grain size distribution $\langle a^3 \rangle = 1.525 \times 10^{-13} \text{ cm}^3$. Knowing the volume density of dust grains, we can estimate the number of sites on the surface of the grains per cm^{-3} as

$$n_d \times n_{\text{sites}} = \quad (8)$$

$$\frac{3 \cdot 0.01 \mu m_H n_{\langle H \rangle}}{4 \pi \langle a^3 \rangle \rho_{\text{gr}}} \times 4 \pi \langle a^2 \rangle \times N_{\text{sites}} = 7.08 \cdot 10^{-8} n_{\langle H \rangle}$$

We assume that no diffusion of water occurs and reactions are limited to the surface. This is a conservative lower limit to the phyllosilicate production since grains will be irregularly shaped and defects at the surface will help water to diffuse into the interior. Assuming the stoichiometry of the following reaction



and that 60% of the surface is silicates and 30% of sites are occupied by water, the lower limit to the number density of phyllosilicates on surfaces is $1.274 \times 10^{-8} n_{\langle H \rangle} \text{ cm}^{-3}$. The fraction of water contained in dust can be written as:

$$\frac{\rho_{\text{water on grain}}}{\rho_{\text{dust}}} = \quad (9)$$

$$\frac{3 \cdot 0.01 \mu m_H n_{\langle H \rangle} \cdot N_{\text{sites}} \cdot 4 \pi \langle a^2 \rangle \cdot 0.6 \cdot 0.3 \cdot 18 m_H}{4 \pi \langle a^3 \rangle \rho_{\text{gr}} \cdot 0.01 \mu m_H n_{\langle H \rangle}}$$

This translates into a lower limit to the fraction of adsorbed water of $\sim 10^{-5}$. If the grains had been all $0.1 \mu\text{m}$ in size, this number would be $\sim 10^{-3}$, two orders of magnitude higher.

Our models show that hydration in meteorites parent bodies (the asteroids) could have occurred in the inner and warm solar nebula. Among different types, CM and CI carbonaceous chondrites typically contain 5–15% $\text{H}_2\text{O}/\text{OH}$ by weight (Rivkin et al. 2002, and references therein) with the least hydrated CVs type showing abundance of hydrogen typically below 0.5 wt% (Beck et al. 2014, and references therein). To account for such large degree of aqueous alteration, subsequent hydration mechanisms need to be considered. For instance, diffusion of water molecules into the silicate bulk enables a higher formation rate of phyllosilicates (Thi et al. 2018, submitted), in particular in those relatively hot regions ($T > 700 \text{ K}$) of the disk midplane where the cluster effect explored in our models does not retain water on the surface efficiently.

5. Conclusions

In this work we have investigated the efficiency of water vapor adsorption onto forsterite grains surfaces as one of the mechanisms that contributed to the water on Earth and in asteroids.

The astrophysical disk model ProDiMo tailored to the solar nebula properties was combined with Monte Carlo simulations of water adsorption on a [100] forsterite crystal lattice. Water vapor abundances, temperature and pressure radial profiles identify the region in the warm disk midplane, between $0.07 - 0.3 \text{ au}$ from the protosun, where hydration of dust grains could have occurred. Several MC simulations were run to assess the dependency of the adsorption rate and the surface coverage on the parameter space identified by the pairs $(T, n_{\text{H}_2\text{O}})$.

Our MC models show that complete surface water coverage is reached for temperatures between 300 and 500 K. For hotter environments (600, 700 and 800 K), less than 30% of the surface is hydrated. At low water vapor density and high temperature, water cluster formation plays a crucial role in enhancing the coverage (see also Appendix C). The binding energy of adsorbed water molecules increases with the number of occupied neighboring sites, enabling a more temperature-stable water layer to form. Lateral diffusion of water molecules lowers the timescale for surface hydration by water vapor condensation by three order of magnitude with respect to an SCT model, ruling out any doubts on the efficiency of such process in a nebular setting.

Finally, the amount of water potentially delivered on Earth drastically varies if we rely on a grain size distribution instead of single sized grains. Grain agglomeration and dust settling to the midplane, the initial steps for planetesimal formation, should clearly lead to a wide grain size distribution as the nebula evolves. In order to improve our initial estimates, detailed dust evolution models should be combined with the water adsorption efficiencies found here.

In addition, dynamical simulations of grain growth are required to understand how agglomeration and collision processes affect the amount of water retained on the grain surfaces and how this competes with the diffusion timescale of water molecules into the bulk of the grains.

Acknowledgements. This work is part of the Dutch Astrochemistry program financed by the Netherlands Organisation for Scientific Research, *NWO*.

References

- Adams, F. C. 2010, *ARA&A*, 48, 47
 Albertsson, T., Semenov, D., & Henning, T. 2014, *The Astrophysical Journal*, 784, 39
 Alexander, C. M. O. ., Newsome, S. D., Fogel, M. L., et al. 2010, *Geochim. Cosmochim. Acta*, 74, 4417
 Amelin, Y., Ghosh, A., & Rotenberg, E. 2005, *Geochim. Cosmochim. Acta*, 69, 505
 Amelin, Y., Wadhwa, M., & Lugmair, G. 2006, in *Lunar and Planetary Inst. Technical Report*, Vol. 37, 37th Annual Lunar and Planetary Science Conference, ed. S. Mackwell & E. Stansbery
 Antonellini, S., Kamp, I., Riviere-Marichalar, P., et al. 2015, *A&A*, 582, A105
 Aresu, G., Meijerink, R., Kamp, I., et al. 2012, *A&A*, 547, A69
 Asaduzzaman, A., Muralidharan, K., & Ganguly, J. 2015, *Meteoritics & Planetary Science*, 50, 578
 Asaduzzaman, A. M., Laref, S., Deymier, P. A., et al. 2013, *Philosophical Transactions of the Royal Society of London A: Mathematical, Physical and Engineering Sciences*, 371
 Barrat, J., Zanda, B., Moynier, F., et al. 2012, *Geochimica et Cosmochimica Acta*, 83, 79
 Beck, P., Garenne, A., Quirico, E., et al. 2014, *Icarus*, 229, 263
 Benisty, M., Juhasz, A., Boccaletti, A., et al. 2015, *A&A*, 578, L6
 Birnstiel, T., Fang, M., & Johansen, A. 2016, *Space Sci. Rev.*, 205, 41
 Boss, A. P. 2004, *The Astrophysical Journal*, 616, 1265
 Bouwman, J., Henning, T., Hillenbrand, L. A., et al. 2008, *ApJ*, 683, 479
 Brearley, A. J. 2006, *The Action of Water*, ed. D. S. Lauretta & H. Y. McSween, 584–624
 Brown, W. A. & Bolina, A. S. 2007, *MNRAS*, 374, 1006
 Cameron, A. G. W. 1995, *Meteoritics*, 30, 133
 Carr, J. S. & Najita, J. R. 2008, *Science*, 319, 1504
 Carr, J. S. & Najita, J. R. 2011, *The Astrophysical Journal*, 733, 102
 Cazaux, S., Bossa, J.-B., Linnartz, H., & Tielens, A. G. G. M. 2015, *A&A*, 573, A16
 Cazaux, S., Cobut, V., Marseille, M., Spaans, M., & Caselli, P. 2010, *A&A*, 522, A74
 Chiang, E. I. 2004, in *Astronomical Society of the Pacific Conference Series*, Vol. 309, *Astrophysics of Dust*, ed. A. N. Witt, G. C. Clayton, & B. T. Draine, 213
 Ciesla, F. J., Lauretta, D. S., Cohen, B. A., & Hood, L. L. 2003, *Science*, 299, 549
 Cuppen, H. M. & Herbst, E. 2007, *The Astrophysical Journal*, 668, 294
 Dartois, E., Ding, J. J., de Barros, A. L.F., et al. 2013, *A&A*, 557, A97
 Davies, J. E. D. 1996, *Journal of inclusion phenomena and molecular recognition in chemistry*, 24, 133
 Davis, S. S. 2005a, *ApJ*, 620, 994
 Davis, S. S. 2005b, *The Astrophysical Journal Letters*, 627, L153
 de Juan Ovelar, M., Pinilla, P., Min, M., Dominik, C., & Birnstiel, T. 2016, *MNRAS*, 459, L85
 de Leeuw, N. H., Parker, S. C., Catlow, C. R. A., & Price, G. D. 2000, *Physics and Chemistry of Minerals*, 27, 332
 Drake, M. J. 2005, *Meteoritics & Planetary Science*, 40, 519
 Dullemond, C. P., van Zadelhoff, G. J., & Natta, A. 2002, *A&A*, 389, 464
 Fegley, Jr., B. 1999, *Space Sci. Rev.*, 90, 239
 Fegley, Jr., B. & Prinn, R. G. 1989, in *The Formation and Evolution of Planetary Systems*, ed. H. A. Weaver & L. Danly, 171–205
 Flaherty, K. M., Hughes, A. M., Teague, R., et al. 2018, *ApJ*, 856, 117
 Gail, H.-P. 2004, *A&A*, 413, 571
 Ganguly, J. & Bose, K. 1995, in *Lunar and Planetary Science Conference*, Vol. 26, *Lunar and Planetary Science Conference*
 Garufi, A., Podio, L., Kamp, I., et al. 2014, *A&A*, 567, A141
 Gavilan, L., Lemaire, J. L., & Vidal, G. 2012, *Monthly Notices of the Royal Astronomical Society*, 424, 2961
 Genda, H. 2016, *GEOCHEMICAL JOURNAL*, 50, 27
 González, B. S., Hernández-Rojas, J., Bretón, J., & Gomez Llorente, J. M. 2007, *J. Phys. Chem. C*, 111, 14862
 Hayashi, C. 1981, *Progress of Theoretical Physics Supplement*, 70, 35

- Helling, C., Woitke, P., Rimmer, P. B., et al. 2014, *Life*, 4
- Hersant, F., Gautier, D., & Huré, J.-M. 2001, *ApJ*, 554, 391
- Howard, K. T., Benedix, G. K., Bland, P. A., & Cressey, G. 2011, *Geochim. Cosmochim. Acta*, 75, 2735
- Huré, J.-M. & Galliano, F. 2001, *A&A*, 366, 359
- Jäger, C., Dorschner, J., Mutschke, H., Posch, T., & Henning, T. 2003, *A&A*, 408, 193
- Kessler-Silacci, J., Augereau, J.-C., Dullemond, C. P., et al. 2006, *The Astrophysical Journal*, 639, 275
- King, H., Stimpfl, M., Deymier, P., et al. 2010, *Earth and Planetary Science Letters*, 300, 11
- Kruijer, T. S., Touboul, M., Fischer-Gödde, M., et al. 2014, *Science*, 344, 1150
- Lesur, G., Kunz, M. W., & Fromang, S. 2014, *A&A*, 566, A56
- Lewis, J. S. 1974, *Science*, 186, 440
- Lin, C. S., Zhang, R. Q., Lee, S. T., et al. 2005, *The Journal of Physical Chemistry B*, 109, 14183, pMID: 16852781
- Makalkin, A. B. & Dorofeeva, V. A. 2009, *Solar System Research*, 43, 508
- Mann, R. K. & Williams, J. P. 2010, *The Astrophysical Journal*, 725, 430
- Mann, R. K. & Williams, J. P. 2012, in *Astronomical Society of India Conference Series*, Vol. 4, *Astronomical Society of India Conference Series*, 35
- Marseille, M. G. & Cazaux, S. 2011, *A&A*, 532, A60
- Min, M., Dullemond, C. P., Kama, M., & Dominik, C. 2011, *Icarus*, 212, 416
- Min, M., Rab, C., Woitke, P., Dominik, C., & Ménard, F. 2016, *A&A*, 585, A13
- Mottl, M., Glazer, B., Kaiser, R., & Meech, K. 2007, *Chemie der Erde / Geochemistry*, 67, 253
- Muralidharan, K., Deymier, P., Stimpfl, M., de Leeuw, N. H., & Drake, M. J. 2008, *Icarus*, 198, 400
- Nuth, III, J. A., Brearley, A. J., & Scott, E. R. D. 2005, in *Astronomical Society of the Pacific Conference Series*, Vol. 341, *Chondrites and the Protoplanetary Disk*, ed. A. N. Krot, E. R. D. Scott, & B. Reipurth, 675
- Pérez, L. M., Isella, A., Carpenter, J. M., & Chandler, C. J. 2014, *ApJ*, 783, L13
- Pinte, C., Dent, W. R. F., Ménard, F., et al. 2016, *ApJ*, 816, 25
- Pirronello, V., Liu, C., Shen, L., & Vidalí, G. 1997, *The Astrophysical Journal Letters*, 475, L69
- Pontoppidan, K. M., Salyk, C., Blake, G. A., & Käufl, H. U. 2010, *The Astrophysical Journal Letters*, 722, L173
- Prigobbe, V., Suarez Negreira, A., & Wilcox, J. 2013, *The Journal of Physical Chemistry C*, 117, 21203
- Rab, C., Güdel, M., Woitke, P., et al. 2018, *A&A*, 609, A91
- Rice, B. M., NoorBatcha, I., Thompson, D. L., & Raff, L. M. 1987, *The Journal of Chemical Physics*, 86, 1608
- Riviere-Marichalar, P., Ménard, F., Thi, W. F., et al. 2012, *A&A*, 538, L3
- Rivkin, A. S., Howell, E. S., Vilas, F., & Lebofsky, L. A. 2002, *Hydrated Minerals on Asteroids: The Astronomical Record*, ed. W. F. Bottke, Jr., A. Cellino, P. Paolicchi, & R. P. Binzel, 235–253
- Salyk, C., Pontoppidan, K. M., Blake, G. A., et al. 2008, *ApJ*, 676, L49
- Schuttlefield, J. D., Cox, D., & Grassian, V. H. 2007, *Journal of Geophysical Research: Atmospheres*, 112, n/a, d21303
- Siess, L., Dufour, E., & Forestini, M. 2000, *A&A*, 358, 593
- Stimpfl, M., Lauretta, D. S., & Drake, M. J. 2004, *Meteoritics and Planetary Science Supplement*, 39
- Stimpfl, M., Walker, A., Drake, M., de Leeuw, N., & Deymier, P. 2006, *Journal of Crystal Growth*, 294, 83
- Thi, W., Hocuk, S., Kamp, I., et al. 2018, *submitted in A&A*
- Thi, W.-F., Mathews, G., Ménard, F., et al. 2010, *A&A*, 518, L125
- Tilling, I., Woitke, P., Meeus, G., et al. 2012, *A&A*, 538, A20
- Velbel, M., Tonui, E., & Zolensky, M. 2012, *Geochimica et Cosmochimica Acta*, 87, 117
- Vicente, S. M. & Alves, J. 2005, *A&A*, 441, 195
- Walsh, C., Millar, T. J., & Nomura, H. 2013, *ApJ*, 766, L23
- Weidenschilling, S. J. 1977, *Astrophysics and Space Science*, 51, 153
- Weisberg, M. K., McCoy, T. J., & Krot, A. N. 2006, *Systematics and Evaluation of Meteorite Classification*, ed. D. S. Lauretta & H. Y. McSween, 19–52
- Willacy, K., Klahr, H. H., Millar, T. J., & Henning, T. 1998, *A&A*, 338, 995
- Woitke, P., Helling, C., Hunter, G. H., et al. 2017, *ArXiv e-prints*
- Woitke, P., Kamp, I., & Thi, W.-F. 2009, *A&A*, 501, 383
- Woitke, P., Min, M., Pinte, C., et al. 2016, *A&A*, 586, A103
- Woitke, P., Riaz, B., Duchêne, G., et al. 2011, *A&A*, 534, A44
- Yamamoto, D. & Tachibana, S. 2016, in *Lunar and Planetary Science Conference*, Vol. 47, 1733
- Young, E. D., Gounelle, M., Smith, R. L., Morris, M. R., & Pontoppidan, K. M. 2011, *ApJ*, 729, 43

Appendix A: H₂ as gas competitor

In the following, we will make some simple estimates to assess the role of dust and H₂ in our Monte Carlo simulations. The simplified approach assumes that we have a constant influx of water molecules onto a fixed surface (representing part of the surface of a single grain). However, the water molecules encounter within a fixed volume other dust grains and H₂ molecules. In a primordial disk, water is typically four orders of magnitude less abundant than H₂. This implies that water will repetitively collide with H₂ before reaching a dust grain, which could change the time scale for water molecules to reach the dust. As H₂ collides frequently with the grain surface it could hinder or block the influx of water. In this study, we consider that H₂ molecules can only be physisorbed on surfaces. H₂ chemisorption is a dissociative process with a high barrier (Rice et al. 1987), which makes the sticking probability of H₂ as two chemisorbed H atoms negligible. We therefore neglect H₂ chemisorption, and consider only the effect of the grains covered by physisorbed H₂ molecules and estimate if this coverage could influence the sticking of water. At the typical gas temperatures considered here, H₂ cannot stick to the warm silicate surface. However, even an extremely short residence time could block that surface site from adsorbing water. The following estimates relate to one representative set of conditions in the disk with $n_{\text{H}_2} = 10^{15} \text{ cm}^{-3}$ and $T_g = 500 \text{ K}$. The size of an adsorption site is assumed to be $(2.6)^2 \text{ \AA}^2$ and the thermal velocity of H₂ molecules is

$$v_{\text{H}_2}^{\text{th}} = \sqrt{\frac{2kT_g}{\pi m_{\text{H}_2}}} = 1.15 \cdot 10^5 \text{ cm/s} . \quad (\text{A.1})$$

The influx of H₂ into a surface site can then be calculated to be

$$F_{\text{H}_2} = n_{\text{H}_2} v_{\text{H}_2}^{\text{th}} (2.6 \cdot 10^{-8})^2 = 7.77 \cdot 10^4 \text{ s}^{-1} . \quad (\text{A.2})$$

At the same time, the influx of water molecules is 2.60 s^{-1} with $v_{\text{H}_2\text{O}}^{\text{th}} = 3.83 \cdot 10^4 \text{ cm/s}$. The residence time on the surface for H₂ molecules is given by the rate constant for adsorption

$$\tau = \frac{1}{\nu^{\text{osc}} \exp(-E^{\text{ads}}/kT_d)} \quad (\text{A.3})$$

with the adsorption energy $E^{\text{ads}}/k \sim 500 \text{ K}$ for H₂ physisorption (Pirronello et al. 1997), the lattice vibrational frequency $\nu^{\text{osc}} = (2n_{\text{surf}}kE^{\text{ads}}/(\pi^2 m_{\text{H}_2}))^{1/2} = 2.50 \cdot 10^{12} \text{ s}^{-1}$, and the density of surface sites $n_{\text{surf}} = 1.5 \cdot 10^{15} \text{ cm}^{-2}$. Assuming furthermore $T_d = T_g$ yields $\tau = 1.08 \cdot 10^{-12} \text{ s}$. If an H₂ molecule would be present on the arrival site of a water molecule, then the water molecule would occupy the place of the H₂ and swap (Cuppen & Herbst 2007). In any case, it has been proven experimentally that a surface covered by H₂ molecule would be more accommodating to incoming species and therefore that the sticking coefficient would be increased. Molecular hydrogen covering a surface serves as a medium to loose kinetic energy and to become more easily thermalised on the surface and adsorb (Gavilan et al. 2012).

Appendix B: Surface potential energy distribution

In the attempt to explain the discrepancies between our results and the ones obtained by Muralidharan et al. (2008),

Table B.1. List of parameters (central adsorption energy, sigma and intensity) of the Maxwell-Boltzmann distributions of surface energy potential models called A , B and C.

E _{bin} (K)	σ	(%)
Model A^a		
19 240 (160)	80	15
15 640 (130)	80	30
8 420 (70)	80	55
Model B		
25 260 (210)	1 000	10
8 420 (70)	4 000	80
0 (0)	4 000	10
Model C		
25 260 (210)	1 000	8
16 840 (125)	500	22
8 420 (70)	1 000	60
3 010 (25)	2 000	10

Notes. Values in (..) are expressed in kJ mol⁻¹. ^(a) Model used in the paper.

we have simulated the water adsorption mechanism on the forsterite [100] crystal plane using three surface energy potential models, called A, B and C (Fig. B.1). These are obtained by three Maxwell-Boltzmann distributions with parameters listed in Table B.1.

Model A (red curve in the left and middle plots of Fig. B.1) is a step function composed by three distributions, where only 45% of the sites have binding energies greater than 14 430 K (120 kJ mol⁻¹), hence those most favorable for attracting the first water molecules (Stimpff et al. 2006).

Model B (green curve) is constructed by matching the surface potential energy distribution shown in Stimpff et al. (2006). Here sites with binding energies smaller than 8 420 K (70 kJ mol⁻¹) are included, contrary to model A.

Finally, the model C (blue curve) includes 8% of surface sites with adsorption energies higher at 25 260 K (210 kJ mol⁻¹), which were not taken into account in model A although claimed by the atomistic model of Stimpff et al. (2006). The surface energy potential distribution of the adsorption sites of the crystal surface determines the coverage of the adsorbed water molecules. As shown in the right plot of Fig. B.1, in model C the surface coverage is 5% higher than in model A at 700 K and $n_{\text{H}_2\text{O}} = 6 \times 10^{10} \text{ cm}^{-3}$. The surface potential energy distribution of model B allows only half the coverage than seen in model A and C, due to the higher hydrophobicity of the surface.

We can conclude that the choice of the sites adsorption energy does not explain the factor of three difference in surface coverage between our work and the Muralidharan et al. (2008) simulations.

Appendix C: Water Cluster simulation

In our MC models the water molecules randomly "walk" on the surface until they adsorb at a favorable site. As two water molecules sit on neighboring sites, a hydrogen bond links the two species, and a dimer can be created with the to-

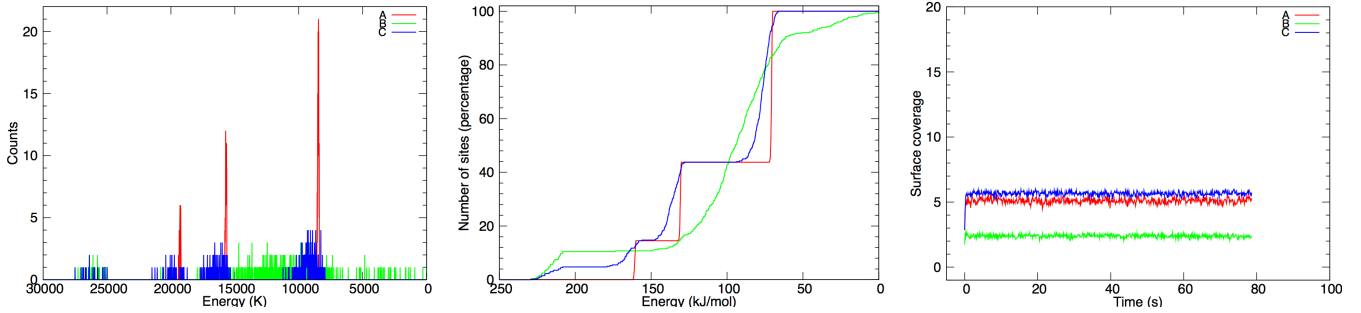


Fig. B.1. Surface potential energy distribution (left plot) and surface sites density (middle plot) of three models: A (red curve), B (green curve) and C (blue curve). The surface coverage for the three models is calculated at 700 K and $n_{\text{H}_2\text{O}} = 6 \times 10^{10} \text{ cm}^{-3}$ (right plot).

tal binding energy higher than the ones of single molecules. This generates the formation of water clusters for which the binding energy increases with increasing size (González et al. 2007). In two dimensions, the binding energies increase with the number of water molecules present in the cluster, while for a 3D cluster Lin et al. (2005) show that the binding energy mainly depends on the number of water molecules close to the surface.

In this work, we used a simple way to calculate the binding energies, which increase linearly with the number of neighboring water molecules (Dartois et al. 2013), but limiting the number of water molecules to four. Water clusters have been implemented in previous MC simulations to study the formation of water on carbon grains in the ISM (Cazaux et al. 2010), to investigate the porous structure of ices (Cazaux et al. 2015) and its effect on the location of the snow line in different astronomical environments (Marseille & Cazaux 2011).

Temperature programmed desorption experiments conducted by Brown & Bolina (2007) confirm that the desorption of pure H_2O ice on a graphite surface occurs at a higher temperature for increasing coverage. Therefore, as the coverage increases, the clusters become more important, and a higher surface temperature is needed to desorb the molecules.

The formation of clusters is therefore a competition between the evaporation of individual water molecules and the encounter of two molecules to initiate the cluster. In our models this effect can be seen in Fig. 5 of Sec. 3.2 and here in Fig C.1. At equal $(T, n_{\text{H}_2\text{O}})$ conditions, 35% of the surface sites are covered by water molecules when they form clusters with neighboring molecules (left plot, pink curve). The binding energies of the adsorbed water increase up to 25000 K (right image) when clusters occur with four neighboring molecules. When the cluster effect is switched off, our simulations show that the surface coverage is 40% reduced (left plot, blue curve) and the adsorbed water molecules possess on average 20000 K binding energy with the surface (middle plot).

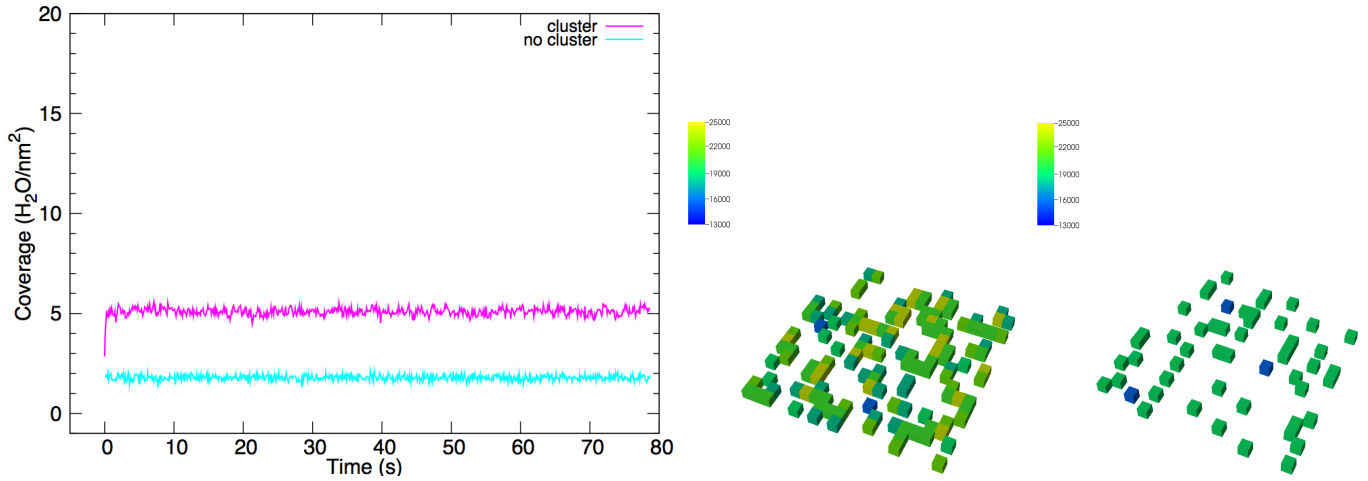


Fig. C.1. Effect of water cluster on surface coverages. On the left, surface coverages ($\text{H}_2\text{O nm}^{-2}$) as a function of time (s) at $n_{\text{H}_2\text{O}} = 6 \times 10^{10} \text{ cm}^{-3}$ and $T = 700 \text{ K}$, with cluster effect (pink curve) and without (light blue curve). On the right, "snapshots" of the grid resembling the [100] forsterite surface showing the adsorption energy of the occupied sites without (middle plot) and with (right plot) cluster effect. The color scale indicates the adsorption energy in the range 13 000 K (blue) - 25 000 K (yellow).